



**HAL**  
open science

## Air-photonics based terahertz source and detection system

Emilien Prost, Vincent Lorient, Eric Constant, Isabelle Compagnon, Luc Bergé, Franck Lépine, Stefan Skupin

► **To cite this version:**

Emilien Prost, Vincent Lorient, Eric Constant, Isabelle Compagnon, Luc Bergé, et al.. Air-photonics based terahertz source and detection system. *The European Physical Journal. Special Topics*, 2023, 232 (13), pp.2157-2166. 10.1140/epjs/s11734-022-00748-7. hal-03920159

**HAL Id: hal-03920159**

**<https://hal.science/hal-03920159v1>**

Submitted on 3 Jan 2023

**HAL** is a multi-disciplinary open access archive for the deposit and dissemination of scientific research documents, whether they are published or not. The documents may come from teaching and research institutions in France or abroad, or from public or private research centers.

L'archive ouverte pluridisciplinaire **HAL**, est destinée au dépôt et à la diffusion de documents scientifiques de niveau recherche, publiés ou non, émanant des établissements d'enseignement et de recherche français ou étrangers, des laboratoires publics ou privés.

# Air-photonics based terahertz source and detection system

Emilien Prost<sup>1\*</sup>, Vincent Loriot<sup>1</sup>, Eric Constant<sup>1</sup>, Isabelle Compagnon<sup>1</sup>, Luc Bergé<sup>2,3</sup>, Franck Lépine<sup>1</sup> and Stefan Skupin<sup>1</sup>

<sup>1\*</sup>Institut Lumière Matière, UMR 5306 Université Lyon 1 - CNRS, Université de Lyon, 69622 Villeurbanne, France.

<sup>2</sup>CEA, DAM, DIF, 91297, Arpajon, France.

<sup>3</sup>Université Paris-Saclay, CEA, LMCE, Bruyères-le-Châtel, 91680, France.

\*Corresponding author(s). E-mail(s): [emilien.prost@univ-lyon1.fr](mailto:emilien.prost@univ-lyon1.fr);

## Abstract

Two-color air plasma based broadband terahertz (THz) generation and subsequent air biased coherent detection (ABCD) of the THz field are presented. Both source and detection system are characterized experimentally and numerically, yielding excellent agreement of measured and simulated signals. We reveal that it is crucial to model the whole optical setup and include the various pump distortions, like temporal and spatial walk-off as well as ellipticity of polarization, in order to interpret the experimental measurements correctly. Moreover, it turns out that geometrical effects in the ABCD scheme shape the recorded THz spectra and need to be taken into account. We confirm that THz electric fields with peak amplitude in the MV/cm range and large spectral bandwidth are produced, allowing us to demonstrate THz spectroscopy with **molecular samples**.

**Keywords:** terahertz generation, plasma, filamentation, ultrashort pulse propagation, spectroscopy

## 1 Introduction

Terahertz (THz) radiation lies in the part of the electromagnetic spectrum usually defined between 0.1 THz and 30 THz. As THz photons are weakly energetic, they do not ionize matter and can only excite free charges, optical phonons in solids and molecular vibrations and rotations occurring over  $\sim$  ps time scales. The past decades have known tremendous technological developments in the elaboration of THz emitters [1–3], particularly linked to the advent of ultrafast laser sources. This technological progress opened up the route of new diagnostics for medical imaging and cancer detection [4], new devices for molecular spectroscopy [5] as well as for greenhouse gas detection and

plant life monitoring [6]. More recently, the production of THz waves operating at high field strengths attracted interest for various applications, e.g., in solid-state physics (see, e.g., the recent review [7]), to probe water dynamics [8], induce ultrafast phase transitions into metastable collective states [9], for THz electron acceleration [10], ultrafast chemistry [11] or even for atom probe tomography [12].

Terahertz time-domain spectroscopy [13–15] (THz-TDS) is one of the most spread applications for pulsed THz radiation. THz-TDS is also used extensively from material science [16] to chemistry [17, 18], so that several commercial systems of this important tool are already available on the market (see [15] and references therein). A major limitation of common THz-TDS systems is

the bandwidth of the THz emitters and detectors, as well as the amplitude of the generated THz fields. The most common emitters and detectors are based on photoconductive antennas or optical rectification in nonlinear crystals. However, their bandwidths are usually below 10 THz due to absorption by optical phonons. Moreover, these solid-state devices are limited by the crystal sizes and their fragility to laser-induced damage.

Consequently, the further development of THz-TDS systems goes hand in hand with the search for suitable and robust THz emitters [3, 19]. An interesting alternative source is based on an air plasma generated by a two-color laser pulse [20–22]. The THz spectra emitted from such plasma are extremely broadband, with ranges up to 75 THz [23] and even beyond [24]. Such a THz source is naturally ultrashort and can be straight-forwardly coupled with air biased coherent detection [25, 26] (ABCD). The use of air as generation and detection medium has several advantages. First, broadband THz fields with high amplitude can be generated. Second, there is no risk of damaging the source or detection medium. The absence of solid materials also means that the occurrence of gaps in the THz spectra due to optical phonons is avoided.

In this paper we report on recent progress in the development and exploitation of a THz platform based on the above mentioned air plasma source and ABCD setup [27]. In Sec. 2 the platform is briefly reviewed, with special emphasis on recent improvements of the signal-to-noise ratio. Rigorous numerical simulations of the whole platform, comprising the key optical elements shaping the input pump pulse, are reported in Sec. 3. Attention is paid to the numerical modeling of the ABCD scheme, from which we reveal and explain important differences between generated and measured THz spectra. By comparing to simplified pump configurations, we identify key parameters of the pump pulse determining the THz yield and spectral shape. Finally, in Sec. 4 we present the performances of the platform by measuring the absorption of D-phenylalanine and thymine samples. The resulting absorption spectra are successfully confronted with Fourier transform infrared (FTIR) measurements.

## 2 Optical setup

To produce a broadband THz radiation we use an air plasma created by a two-color ultra-short laser pulse [20–22]. The two-color pulse composed of fundamental (FH) and second harmonic (SH) ionizes the gaseous medium, here mostly dioxygen molecules. Acceleration of the free electrons by the two-color laser electric field leads to an asymmetric current containing a low frequency component that acts as radiation source in the THz spectral range [23, 28]. The detection of the THz radiation is performed by air biased coherent detection (ABCD) [25, 29, 30]. This technique relies on four wave mixing in air between the THz field, a DC bias field and a FH probe field. The produced SH radiation is detected and contains the information about the THz field.

The optical setup presented in Fig. 1 is an improved version of the one used in Ref. [27]. We use a Ti:Sapphire chirp-pulse amplifier that produces pulses of 30 fs at a repetition rate of 5 kHz with a central wavelength of 800 nm. Only 20 % of the total energy output of the amplifier is used for our experiments, which corresponds to 350  $\mu$ J. This initial FH beam is split between two arms, the first one (74%) is used for the THz generation and the second one (26%) for the ABCD detection. Compared to our previous work [27] the energy ratio between the generation and detection arm has been adjusted. On one hand, the increase in energy on the first arm leads to an enhancement of the THz yield. On the other hand, lower energy for the detection prevents any plasma formation in the ABCD detection, thus making it more stable. To get rid of water vapor, which presents strong absorption lines in the THz range, the whole beam-path of the THz field is placed in a dry air enclosure (see gray area on Fig.1).

To produce our two color laser pulse, we use second harmonic generation (SHG) in a 100  $\mu$ m thick  $\beta$ -barium borate (BBO) crystal. This crystal is cut such that type I phase matching is optimized. At the output of the crystal, the SH pulse is orthogonally polarized with respect to the FH polarization. We use an ultra-thin half-waveplate at 800 nm (quartz, 45 $\mu$ m thickness) to turn the polarization axis of the FH pulse parallel to the SH polarization axis. This waveplate acts as an approximate full waveplate for the SH component, thus rendering the polarization of the SH

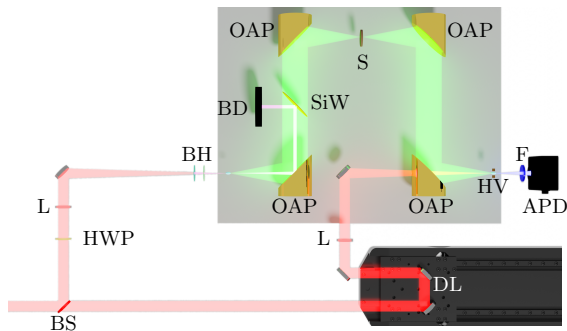


**Fig. 1** Schematic of the THz platform. BS : Beam splitter (76% reflection); L : focusing lens ( $f = 300$  mm); DL : Delay line; HWP : Half waveplate; BH : composed of a BBO crystal and a dual wavelength waveplate; BD : Beam dump; SiW : Silicon wafer; S : Sample; HV : High voltage electrodes; F : 400 nm band-pass filter; APD : Avalanche photodiode. The area in gray indicates the dry air enclosure.

pulse almost unchanged and only slightly elliptical. Both optics are placed before the geometrical focus of the lens, with the distance between BBO and focus being about 7 cm.

This two color laser pulse produces a plasma that is located a few millimeters before the geometrical focus of the lens. Oscillation of the free electrons inside the plasma gives rise to THz radiation that is collected and collimated by a gold coated off-axis parabolic mirror (OAP). A silicon wafer, placed in the collimated beam path, is used to filter out the two color optical pulse while transmitting 50% of the THz power [31]. A second OAP is used to focus the THz field onto the sample. A second pair of OAPs collects and focuses the THz field for the detection between the high voltage electrodes of the ABCD setup.

The part of the laser pulse used as a probe for the ABCD scheme goes through a delay line, which allows to control its delay  $\tau$  with respect to the incoming THz pulse on the fs time-scale. The probe pulse is then focused by a lens through a hole in the last OAP, such that both foci of THz and probe pulses overlap. Note that the half waveplate located in the pump arm, before the focusing lens, renders the polarization of THz pulse and probe pulse parallel. The high voltage electrodes are used to apply a static bias field in the same direction as the pulses polarization.

Our detection scheme relies on four wave mixing mediated by the third order nonlinearity in air. The mixing process produces a SH pulse and

involves the FH probe field  $E_\omega$  and a low frequency field  $E_\Omega = E_{\text{THz}} + E_{\text{bias}}$ , composed of the sum of THz and bias field. We use a bandpass filter to isolate the SH pulse and detect it with an avalanche photodiode. The resulting SH signal  $S_{2\omega}$  on the photodiode depends on the delay  $\tau$ , and by neglecting the finite duration of the probe pulse, the signal can be expressed as [25]

$$S_{2\omega}(\tau) \propto I_\omega^2 [E_{\text{THz}}^2(\tau) + E_{\text{bias}}^2 + 2E_{\text{THz}}(\tau)E_{\text{bias}}], \quad (1)$$

with  $I_\omega$  being the intensity of the FH probe pulse. To extract the THz field  $E_{\text{THz}}(\tau)$  from the SH signal we perform two successive measurements,  $S_{2\omega}^+$  and  $S_{2\omega}^-$ , while applying static bias fields of opposite signs. The difference of those two measurements

$$S_{\text{THz}}(\tau) = S_{2\omega}^+(\tau) - S_{2\omega}^-(\tau) \propto I_\omega^2 E_{\text{THz}}(\tau) |E_{\text{bias}}| \quad (2)$$

is directly proportional to the THz field.

In this regards, the acquisition electronics has been improved compared to the one previously reported in [27]. We adapted the time constant of our high voltage supplies, allowing us to increase the high voltage sign switch frequency while keeping the same stability on the high voltage output. We also replaced the 10 bits analog to digital converter integrated in our micro-controller by an external 15 bits one (ADS1115). This enhances the resolution and sensitivity of our detection significantly and gives us the opportunity to perform statistics on several measurements, while previously averaging over several measurements were performed to oversample the signal. This upgrade of the acquisition electronics coupled with the adjustment of the energy ratio between the pump and probe arms of the experiment gives a better overall stability with an improved resolution and sensitivity of the acquisition.

The measured THz pulses are almost single cycle with an envelope of about 50 fs FWHM duration. The measurements are performed with a bias field of  $E_{\text{bias}} = \pm 10$  kV/cm with steps of 5 fs over a span of 10 ps. By comparing the signal of the photodiode with and without bias field applied [32], we measure a THz electric field strength of 1 MV/cm. Using the protocol described in [33] we estimate the signal to noise

ratio (SNR) and dynamic range (DR) of our acquisition to 350 and  $10^4$ , respectively. These estimations were performed in the temporal domain directly on the signals measured by the acquisition electronics, that is,  $S_{2\omega}$  given by Eq. (1). **Switching to a 15 bits analog to digital converter allows us to perform statistics on our acquisitions. By measuring the mean amplitude of the signal and its standard deviation, we calculate the SNR as the ratio between the two. The DR is calculated as the ratio between the maximum amplitude of the signal and the standard deviation of the noise signal. The noise signal is taken as the signal in absence of the THz field, in our case we measure it at long negative delays, that is, before the THz pulse arrival.**

### 3 Numerical simulations

In this section, we present comprehensive numerical simulations of the different stages of our THz platform. Special efforts were made to meet the same field configurations as in the experiments, that is, propagation effects in all optical components after the focusing lens are taken into account. In particular, walk-off effects in the BBO crystal, in the dual wavelength plate as well as in the free air propagation turn out to be crucial for a proper characterization of the system. The air-plasma based THz source is modelled by a vectorial version of the unidirectional pulse propagation equation (UPPE) [34, 35] that governs the forward-propagating transverse electric field  $\vec{E} = (E_x, E_y)$  of elliptically-polarized pulses

$$\partial_z \hat{E} = i\sqrt{k^2(\omega) - k_x^2 - k_y^2} \hat{E} + i\frac{\mu_0\omega^2}{2k(\omega)} \hat{P}_{\text{Kerr}} - \frac{\mu_0\omega}{2k(\omega)} \left( \hat{J} + \hat{J}_{\text{loss}} \right). \quad (3)$$

We use such vectorial model to take into account the slightly elliptical polarization of the two-color pump induced by the ultra-thin waveplate. In Eq. (3),  $\hat{E}(k_x, k_y, z, \omega)$  is the Fourier transform of the transverse laser electric field with respect to  $x$ ,  $y$ , and  $t$ . The longitudinal laser electric field component  $E_z$  is neglected for the moderate focusing conditions used in the experiments. The square-root on the right-hand side of Eq. (3) describes linear dispersion and diffraction of the

pulse, where  $k(\omega) = \omega n(\omega)/c$  contains the frequency dependent refractive index  $n(\omega)$  of air. The other terms contain the third-order nonlinear polarization

$$\vec{P}_{\text{Kerr}}(t) = \epsilon_0 \chi^{(3)} E^2(t) \vec{E}(t), \quad (4)$$

with Kerr index  $n_2 = 3\chi^{(3)}/4n_0^2 c \epsilon_0$ . Dispersion of  $\vec{P}_{\text{Kerr}}$  is neglected, that is,  $\chi^{(3)}$  is taken as constant in the relevant frequency window, and consistently  $n_0 = n(\omega_{\text{FH}})$  is used in the prefactor. The electron current  $\vec{J}$  follows from a Drude model

$$\partial_t \vec{J}(t) + \nu_c \vec{J}(t) = \frac{q_e}{m_e} N_e(t) \vec{E}(t), \quad (5)$$

and a loss term  $\vec{J}_{\text{loss}}(E, N_e)$  due to ionization [36–38]. The free electron density  $N_e$  is governed by

$$\partial_t N_e(t) = W(E)[N_a - N_e(t)] \quad (6)$$

with field dependent ionization rate  $W(E)$  and density of neutral species  $N_a$  to be ionized<sup>1</sup>. In Eq. (5),  $q_e$  and  $m_e$  are the electron charge and mass, respectively, and  $\nu_c$  denotes the electron-neutral collision rate. More details about this model can be found in [39] while the physical parameters for air are taken from [40].

The simulations employ the same laser parameters as our experiments, namely an incident linearly polarized 240  $\mu\text{J}$  laser pulse at 800 nm with 30 fs FWHM duration and 6 mm FWHM spatial beam width on the focusing lens  $L$  with  $f = 30$  cm. This fundamental harmonic (FH) pulse is then frequency doubled in the 100  $\mu\text{m}$ -thick BBO crystal situated 7 cm before the linear focus point. An orthogonally polarized co-propagating second harmonic (SH) pulse is created (5.5% energy conversion), where, in contrast to previous works [41], both spatial and temporal walk-off are taken into account by solving

$$i[\partial_z + \delta_\tau \partial_\tau - \delta_x \partial_x] A_{\text{SH}} + \chi A_{\text{FH}}^2 e^{i\Delta kz} = 0, \quad (7)$$

$$i\partial_z A_{\text{FH}} + \chi A_{\text{FH}}^* A_{\text{SH}} e^{-i\Delta kz} = 0, \quad (8)$$

for the slowly varying envelopes  $A_{\text{SH}}$  and  $A_{\text{FH}}$  expressed in a reference frame co-moving with

---

<sup>1</sup>For our laser configuration only oxygen molecules, which have the lowest ionization potential of main air constituents, get ionized.

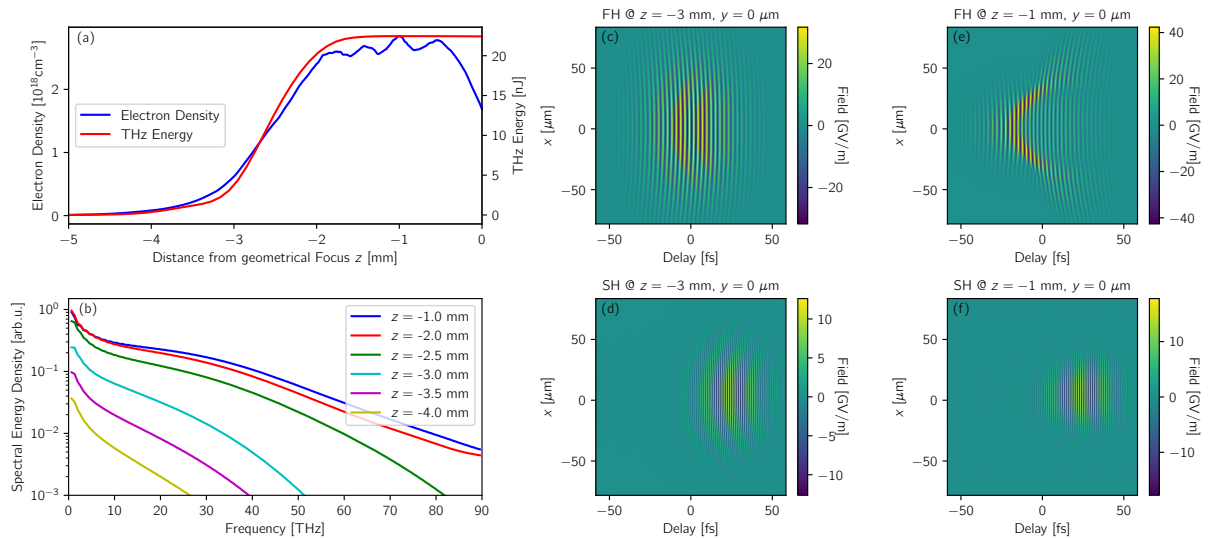


**Fig. 2** THz source: (a) Peak plasma density and THz energy ( $\nu < 90$  THz) versus propagation distance relative to the geometrical focus at  $z = 0$ . (b) Snapshots of the transverse integrated THz spectrum at several positions  $z$  along the plasma. Snapshots of the main FH (c) and SH (d) polarization component of the pump field near the beginning of the plasma at  $z = -3$  mm. (e) and (f) show the same fields inside the plasma after THz generation has stopped due to lack of temporal overlap between SH and FH component at  $z = -1$  mm.

the FH pulse (retarded time  $\tau$ ). The symbol  $\chi$  comprises the effective  $\chi^{(2)}$  nonlinearity,  $\Delta k = 2k_{\text{FH}} - k_{\text{SH}}$  is the phase mismatch, and  $\delta_\tau = 1/v_{\text{g}}^{\text{SH}} - 1/v_{\text{g}}^{\text{FH}}$  is the group velocity mismatch responsible for temporal walk-off. For type-I SHG the SH pulse is extraordinarily polarized, that is, both  $k_{\text{SH}}$  and  $v_{\text{g}}^{\text{SH}}$  depend on the angle between propagation direction (wave vector) and optical axis of the uniaxial BBO crystal. This angle is chosen to 0.510 rad, such that the phase mismatch  $\Delta k = 0$  vanishes. Spatial walk-off is characterized by the walk-off angle  $\delta_x$ , that is, the angle between propagation direction (wave vector) and Poynting vector of the SH beam. Note that we defined the coordinate system such that spatial walk-off goes in  $x$  direction. For evaluating the relevant parameters  $\delta_\tau$  and  $\delta_x$  we used the BBO dispersion relation given in Ref. [42], yielding  $\delta_\tau = 1.93 \times 10^{-10}$  s/m and  $\delta_x = -0.678$  rad.

After passing through the BBO crystal, the polarization of the FH and SH pulses is aligned by means of a 45  $\mu\text{m}$  thick dual wavelength waveplate made of quartz. Because of the waveplate configuration, no spatial walk-off takes place. We ignore any nonlinear effects in the waveplate but take into account the temporal walk-off  $\delta_\tau = 2.17 \times 10^{-10}$  s/m using the quartz dispersion relation given in Ref. [43].

At a distance of about 4 mm before the geometrical focus, here denoted by  $z = 0$ , the two-color pump intensity exceeds the threshold for ionization and an air-plasma is produced. Therefore, we start the computationally expensive UPPE simulation solving Eq. (3) at  $z = -5$  mm. All other pump propagation after the lens, including SHG in the BBO, polarization rotation in the waveplate, and linear propagation in air is computationally light and handled by a pre-processor. We neglect the effect of the Kerr nonlinearity on the pulse propagation in the pre-processor. The value of the  $B$ -integral at  $z = -5$  mm is smaller than one, and we checked that starting the UPPE simulation at  $z = -10$  mm, which reduces the  $B$ -integral by about a factor two, yields no significant differences. Figure 2(a) shows the resulting simulated peak electron density versus the propagation distance  $z$ . In the same figure, the energy build-up of the generated spectral components below 90 THz is plotted. Note that this electron density response and THz energy yield differ from those reported in [27] because of a higher input beam energy and fraction of second harmonic. Interestingly, THz generation stops well before the end of the plasma zone. Before explaining this observation, it is worth noticing that the generated THz spectrum broadens significantly during the

generation process, as shown in Fig. 2(b). Higher frequencies generated later along the propagation path, that is, farther away from the beginning of the plasma.

As already indicated above, the pre-processor takes into account the dispersion properties of the BBO, of the quartz dual wavelength waveplate as well as of the ambient air. This is crucial in order to get the correct beam and pulse profile as well as its (slightly elliptic) polarization state. In particular the temporal walk-off between the two pulse components turns out to be of utmost importance, **in agreement with** [44]. To get further insight, the main FH and SH field components at the beginning ( $z = -3$  mm) and at the end ( $z = -1$  mm) of the region where THz radiation is generated are shown in Fig. 2(c)-(f). The orthogonal field components (not shown) are about one order of magnitude smaller. Obviously, the SH pulse is delayed by about 25 fs compared to the FH pulse, thus, the delay is of the order of the pulse duration itself. At  $z = -3$  mm the two components overlap near zero delay, and the photocurrent mechanism for THz generation is active. At  $z = -1.5$  mm, however, plasma defocusing in the trailing part of the FH pulse has completely separated the two colors in the spatio-temporal domain. This is the reason why THz generation stops roughly in the middle of the plasma at  $z = -1.5$  mm, and the simulated THz energy yield remains of the order of few tens of nJ.

Figure 3(a) shows the spatial evolution of the THz fluency in the source area. During the main THz production stage  $z < -1.5$  mm the THz beam is bell-shaped, but then it quickly evolves into the typical ring structure of conical emission [45]. The final THz spectral energy density at the end of the THz production stage ( $z = -1$  mm) in Fig. 3(b) suggests that this broadband source could be used for spectroscopy in the range of 1 to 50 THz and beyond.

Finally, we want to shed some light on the THz detection process, that is, the part of the generated THz field that we can detect in our ABCD measurements. One could naively expect to measure a pattern close to the final spectrum at the end of the plasma in Fig. 3(b). This is, however, not the case. Both high and low THz frequencies are strongly suppressed in the ABCD scheme for the following two reasons.

First, the finite duration of the probe pulse (here 30 fs FWHM duration) poses an upper bound to the detectable THz frequencies [46, 47]. In the equation for the ABCD THz signal Eq. (2) the convolution with the temporal envelope of the probe pulse is omitted for simplicity. Taking this into account, one finds for the THz signal

$$S_{\text{THz}}(\tau) \propto |E_{\text{bias}}| \int I_{\omega}^2(t - \tau) E_{\text{THz}}(t) dt. \quad (9)$$

In temporal Fourier domain this implies that the THz spectrum  $\hat{E}_{\text{THz}}(\omega)$  gets multiplied by the Fourier transform of  $I_{\omega}^2(t)$ , that is, the longer the probe pulse duration, the more narrow the accessible spectral window. For our configuration, frequencies above 30 THz are strongly suppressed by the ABCD temporal optical resolution, as can be appreciated when comparing Figs. 4(b) and 3(b). Any features which affect this spectral region, e.g., the influence of a chirp in the pump pulse as reported in Ref. [27], are thus not detectable in the present experimental configuration.

Second, the spectrum shown in Fig. 3(b) is spatially integrated over the transverse plane. In contrast to that, the ABCD setup detects only the part of the THz field overlapping with the focused IR probe pulse and the high voltage field. This is also reflected by Eq. (9) when one remembers that both  $I_{\omega}$  and  $E_{\text{THz}}$  depend on spatial variables as well. Therefore, it is instructive to compute the THz field as it would appear in the detection area between the two electrodes. The four parabolic mirrors are essentially forming two consecutive 4f systems. Thus, an image of the THz source is produced. The resulting evolution of the THz fluence versus the propagation distance is shown in Fig. 4(a). Here, the 50% transmittance of the silicon wafer is taken into account. For convenience, the position of the image of the geometrical focus of the laser pump is set to  $z = 0$ , which makes it easier to compare with Fig. 3. The highest THz fluency (and intensity) in the detection area, as shown in Fig. 4(a), is obtained at  $z = -2.5$  mm. This corresponds to the position of maximum THz generation in the source area, cf. Figs. 2 and 3. As already mentioned, in order to perform ABCD measurements it is crucial to have a good overlap between THz and IR probe pulse. In the experiments, the probe pulse focus position is adjusted such that the ABCD signal is maximized. It is

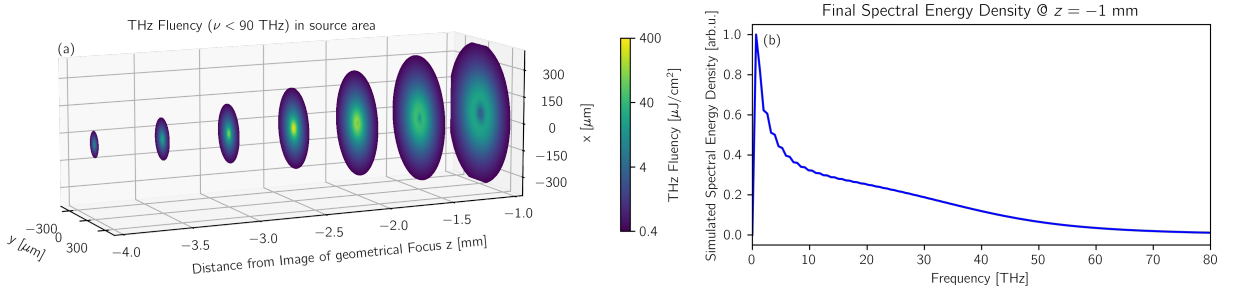


**Fig. 3** THz source: (a) THz fluency ( $\nu < 90$  THz) in the source area as a function of the propagation distance. The position of the geometrical focus of the pump laser is denoted with  $z = 0$ . (b) Transverse integrated THz spectrum at  $z = -1$  mm, that is, at the end of the zone of THz generation [same as the blue curve in Fig. 2(b), but in linear scale].

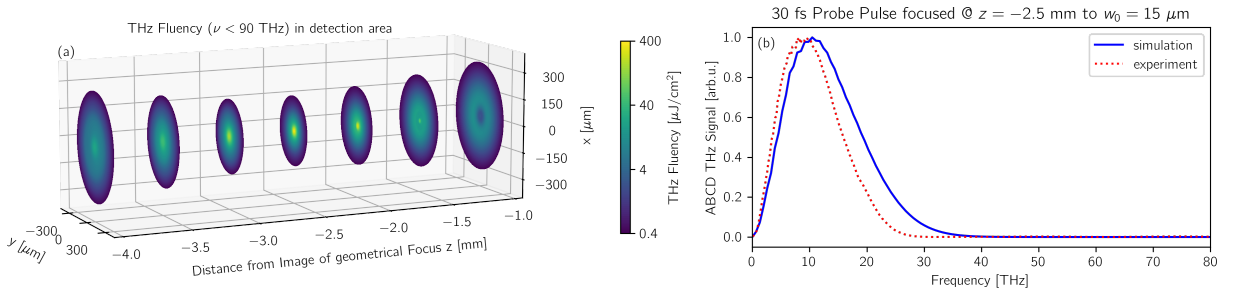


**Fig. 4** THz detection: (a) THz fluency ( $\nu < 90$  THz) in the detection area between the HV electrodes as a function of the propagation distance. The position of the image of the geometrical focus of the pump laser is denoted with  $z = 0$ . (b) Spectrum from a simulated ABCD method involving a 30 fs probe pulse focused to 15  $\mu\text{m}$  waist at  $z = -2.5$  mm (see text). The experimental spectrum taken at a relative humidity below 5% inside the enclosure is shown as red dotted line.

therefore reasonable to assume that the IR probe pulse is focused at the THz fluency maximum at  $z = -2.5$  mm. The probe pulse focal FWHM spot size can be estimated to be less than 20  $\mu\text{m}$ , that is, much smaller than the THz spot-size. Thus, only a small fraction of the THz field, close to the optical axis, actually contributes to the detection process. To account for this spatial overlap we modify the integral in Eq. (9) to

$$S_{\text{THz}}(\tau) \propto \int I_{\omega}^2(t - \tau, x, y) E_{\text{THz}}(t, x, y) dt dx dy,$$

where we assume that the THz signal  $S_{\text{THz}}$  mainly originates from near the probe focal plane and thus ignore integration along  $z$ . Because the THz spot size is strongly frequency dependent, this leads to suppression of lower THz frequencies in the ABCD scheme. A similar effect was reported for THz detection via electro-optical sampling in [48]. Besides, parts of the low frequency field may not be collected by the parabolic mirror because beam divergence increases with decreasing frequency. This suppression of THz frequencies

below 10 THz can be clearly seen in the simulated ABCD signal shown in Fig. 4(b), in particular when it is compared to the spectral energy density emitted by the source in Fig. 3(b).

The simulated ABCD spectrum is in excellent agreement with the experimental spectrum shown as a red dotted line in Fig. 4(b), obtained by taking the Fourier transform of the measured time dependent THz signal. The experimental spectrum exhibits a smooth profile extending from 1 THz to 30 THz, slightly narrower than the simulated one. We attribute this discrepancy to uncertainties in the laser pulse (probe) duration. Even at this humidity level, water absorption lines can still be seen between 5 THz and 10 THz [49]. For this measurement, we used an average over 5 laser shots for each data point, which results in an acquisition time of about 10 minutes.

Before presenting THz-TDS results obtained with the platform it is worth to shed light on the impact of the pump configuration on both THz spectra and measured ABCD signals. To this end, we performed several simulations employing

simplified synthetic two-color pump pulses as initial datum for the UPPE simulations starting at  $z = -5$  mm as already mentioned above. The synthetic pump pulses neglect any previous propagation effects in the optical setup (except linear focusing), and the SH pulse profile is just proportional to the square of the FH pulse profile. We only allow two control parameters which turned out to have crucial impact on the THz generation, namely, the temporal separation between SH and FH pulse  $\tau$  and phase-angle  $\phi$  between SH and FH carrier wave. From the original pump field computed by the aforementioned pre-processor we extracted  $\tau \approx 25$  fs and  $\phi \approx \pi/2$  as closest match for the synthetic pump field at  $z = -5$  mm (see also pump snapshots shown in Fig. 2). The resulting THz spectrum in the source area is shown as the black dashed line in Fig. 5(a). Obviously, the THz spectral shape is not very different compared to the original one (solid blue line), but the yield is reduced by roughly a factor five. We checked that this difference in the THz yield is due to a slightly larger SH pulse duration and thus a better overlap for the original pump configuration. The similarity of the spectral shape however comes from the matching of the phase angle  $\phi$ . The same synthetic pulse but with a phase angle  $\phi = 0$  produces a quite distinct spectrum, as can be inferred from the black dotted line in Fig. 5(a). By contrast, removing the temporal separation by setting  $\tau = 0$  increases the THz yield by more than one order of magnitude and enlarges the spectral extend (black dashed-dotted line), underlining once more the importance of this parameter. Other features of the original pump profile, like deviation from linear polarization and slight spatial misalignment can be seen in the THz field profiles (not shown) but are of minor influence on the THz yield and spectral energy density.

Finally, it is worth checking if the above modifications of the THz spectra would be detectable by the ABCD scheme on our platform. Figure 5(b) shows the resulting simulated signals for our 30 fs probe pulse. Color codings are the same as in Fig. 5(a). As we have already seen above, the high frequency part  $> 30$  THz is completely lost, so that the spectral shapes of all curves become very similar. Some variations due to changes in the phase angle survive, however, they are not very significant. Merely the significant differences in the

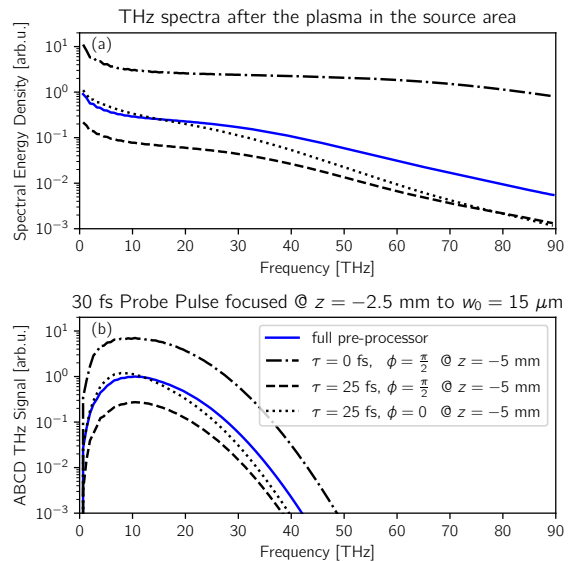


**Fig. 5** Impact of pump distortions on the THz spectra in (a) the source area and (b) on the ABCD signal. The blue lines show the spectra as reported in Fig. 3(b) and Fig. 4(b) but in logarithmic scale, respectively. The black lines show what happens when the pump pulse at  $z = -5$  mm is replaced by a synthetic two-color pulse with delay  $\tau$  and phase-angle  $\phi$  as indicated in the legend (see text for details).

THz yield are clearly visible in the ABCD THz signal, as expected. Using significantly shorter probe pulses than the 30 fs employed in our setup would render the ABCD method capable of detecting those shape differences.

## 4 Time-domain spectroscopy

The THz platform allows to perform THz-TDS by placing a sample at the intermediate focus in the THz beam path. To demonstrate this capability of the improved setup, we use *D*-phenylalanine and thymine samples. Crystalline powders were obtained from Sigma-Aldrich, with purities of 98% and 99%, respectively. Our samples have been prepared by deposition of the molecules on small pieces of silicon wafer ( $\sim 1$  cm<sup>2</sup>). This deposition was performed by sublimating some powder under vacuum, while maintaining the temperature below the melting point.

For those measurements, the temporal step-size in the ABCD is reduced to 2 fs to improve the resolution of the signal in temporal domain, thus expanding the spectral span to 250 THz, and the averaging is performed over 10 laser shots per

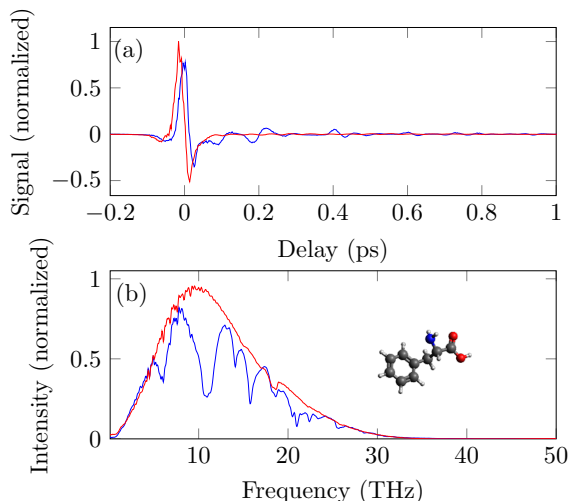


**Fig. 6** (a) Temporal profile of the THz electric field with a sample of D-phenylalanine deposited on a silicon wafer (blue curve) and without deposition on the silicon wafer as reference (red curve). Both spectra are normalized to the reference spectrum peak value. (b) Retrieved intensity spectra with the same color code.

data point. To keep the acquisition time below 30 minutes the temporal span is reduced to 5 ps, which increases the spectral step-size to 0.2 THz. Figure 6(a) shows the resulting temporal profile of the THz electric field for D-phenylalanine, together with a reference measurement of a clean piece of silicon wafer. The strong modification of the THz pulse by the propagation through the deposited D-phenylalanine is clearly visible. The most noticeable change is the (small) delay of the main pulse caused by the different group velocity inside the sample. Furthermore, a stretching of the signal induced by absorption and dispersion in the sample leads to an oscillation like pattern, as can be seen between 0.1 and 0.6 ps. Once transformed to the spectral domain, those temporal modifications result in absorption bands between 5 THz and 30 THz, see Fig. 6(b). As in the reference measurement shown in Fig. 4(b), the relative humidity was kept below 5%, nevertheless, spectral lines attributed to water can still be observed below 10 THz. The absorption line at 18 THz appears due to a phonon overtone in the silicon wafer [31].

To distinguish the absorption lines induced by the molecular samples from the ones coming from environment and substrate, we normalize the transmission spectra by dividing the measured

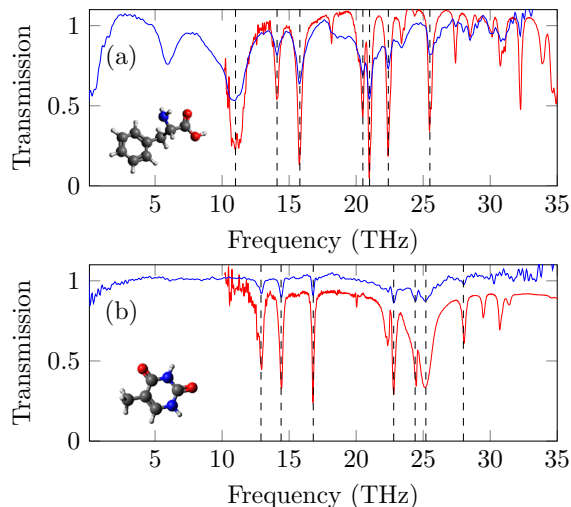


**Fig. 7** Reconstructed transmission spectrum with (a) D-phenylalanine and (b) thymine samples. The blue lines correspond to the spectra measured by THz-TDS and the red ones to measurements done with a FTIR spectrometer. The vertical dashed lines are a guide for the eye indicating the main line positions.

sample spectrum by the above mentioned reference spectrum of a clean piece of silicon wafer. The reconstructed transmission spectra obtained for D-phenylalanine and thymine samples are shown in Fig. 7(a) and (b) respectively. We can notice that the small amplitudes lines attributed to water vapor absorption below 10 THz and the absorption line at 18 THz, visible in Fig 6(b), do not appear anymore. Here we will only discuss the lines below 30 THz, above this frequency the measured absorption spectra drop to the noise level, as can be seen on Fig. 6(b). We compare the measured transmission spectra with measurements taken with a Fourier Transform Infra-Red (FTIR) spectrometer (Bruker Invenio) of the same samples in the overlapping spectral region above 10 THz. We notice that the main line positions, indicated by the dashed vertical lines on Fig 7, agree very well with the FTIR measurement for both molecular samples. Deviations are well below the spectral resolution of the THz measurements (0.2 THz). The THz measurements give moreover access to frequencies below 10 THz, as can be observed in Fig. 7(a) around 6 THz.

## 5 Conclusion

In this paper, we have presented a detailed characterization of an air photonics based terahertz platform and its ability to perform absorption spectroscopy in bio-relevant molecular samples. The whole platform, including the detection scheme, was carefully benchmarked against comprehensive numerical simulations. This confrontation of theoretical results and measurements performed on our setup revealed that it is important to take into account pulse and beam shaping effects in the setup even before the plasma for THz generation is formed. In particular, walk-off effects in the SHG process as well as along the full beam path (e.g., waveplate and two-color propagation in air) turned out to be crucial, because they alter the spatio-temporal overlap of the two pump colors in the plasma significantly. Moreover, we showed that the THz spectra retrieved by ABCD measurements are strongly dependent on the probe characteristics, namely its spatial and temporal extends. While the latter determines the high-frequency cut-off of the measurable THz spectrum, the former one sets a limit on the low frequency part.

With the upgraded precision of the acquisition electronics, we report a signal to noise ratio of above 300 and a dynamic range of  $10^4$ , in the temporal domain, which makes our platform suitable for THz time-domain spectroscopy. We demonstrate this capability by measuring **transmission spectra of D-phenylalanine and Thymine samples**. Because of its simple layout, other types of applications employing THz pulses as pump or probe such as THz streaking [50], molecular orientation [51] or nonlinear spectroscopy [52] are possible.

**Acknowledgments.** We thank B. Moge, I. Aguilí, F. Khalid Balyos and C. Clavier for technical support. We thank P. U. Jepsen and B. Zhou from the Technical University of Denmark for fruitful discussions. We acknowledge financial support from CNRS and the ANR ALTESSE2 (ANR-19-ASMA-0007) project. S. Skupin thanks the Qatar National Research Fund (NPRP 12S-0205-190047) for support. Numerical simulations were performed using resources at Grand Équipement National De Calcul Intensif (GENCI) (A0100507594).

## Statements and Declarations

### Conflict of Interest

The authors have no conflicts to disclose.

### Data Availability Statement

The data that support the findings of this study are available from the corresponding author upon reasonable request.

## References

- [1] Tonouchi, M.: Cutting-edge terahertz technology. *Nature Photonics* **1**(2), 97–105 (2007). <https://doi.org/10.1038/nphoton.2007.3>
- [2] Redo-Sanchez, A., Laman, N., Schulkin, B., Tongue, T.: Review of terahertz technology readiness assessment and applications. *Journal of Infrared, Millimeter, and Terahertz Waves* **34**(9), 500–518 (2013). <https://doi.org/10.1007/s10762-013-9998-y>
- [3] Zhang, Y., Li, K., Zhao, H.: Intense terahertz radiation: generation and application. *Frontiers of Optoelectronics* **14**(1), 4–36 (2021). <https://doi.org/10.1007/s12200-020-1052-9>
- [4] Yu, C., Fan, S.T., Sun, Y.W., Pickwell-Macpherson, E.: The potential of terahertz imaging for cancer diagnosis: A review of investigations to date. *Quant. Imaging, Med. Surg.* **2**, 33–45 (2012)
- [5] Bergé, L., Kaltenecker, K., Engelbrecht, S., Nguyen, A., Skupin, S., Merlat, L., Fischer, B., Zhou, B., Thiele, I., Jepsen, P.U.: Terahertz spectroscopy from air plasmas created by two-color femtosecond laser pulses: The ALTESSE project. *Eur. Phys. Lett.* **126**(2), 24001 (2019)
- [6] Gente, R., Koch, M.: Monitoring leaf water content with THz and sub-THz waves **11**, 15 (2015)
- [7] Salén, P., Basini, M., Bonetti, S., Hebling, J., Krasilnikov, M., Nikitin, A.Y., Shamuilov, G., Tibai, Z., Zhaunerchyk, V., Goryashko,

- V.: Matter manipulation with extreme terahertz light: Progress in the enabling thz technology **838-837**, 1–74 (2022)
- [8] Novelli, F., Guchhait, B., Havenith, M.: Towards Intense THz Spectroscopy on Water: Characterization of Optical Rectification by GaP, OH1, and DSTMS at OPA Wavelengths. *Materials* **13**(6), 1311 (2020)
- [9] Li, X., Qiu, T., Zhang, J., Baldini, E., Lu, J., Rappe, A.M., Nelson, K.A.: Terahertz field-induced ferroelectricity in quantum paraelectric SrTiO<sub>3</sub>. *Science* **364**(6445), 1079–1082 (2019)
- [10] Nanni, E.A., Huang, W.R., Hong, K.-H., Ravi, K., Fallahi, A., Moriena, G., Dwayne Miller, R.J., Kärtner, F.X.: Terahertz-driven linear electron acceleration. *Nat. Commun.* **6**, 8486 (2015)
- [11] LaRue, J.L., Katayama, T., Lindenberg, A., Fisher, A.S., Öström, H., Nilsson, A., Ogasawara, H.: Thz-pulse-induced selective catalytic co oxidation on ru. *Phys. Rev. Lett.* **115**, 036103 (2015)
- [12] Vella, A., Houard, J., Arnoldi, L., Tang, M., Boudant, M., Ayoub, A., Normand, A., Da Costa, G., Hideur, A.: High-resolution terahertz-driven atom probe tomography. *Sci. Adv.* **7**(7), 7259 (2021)
- [13] Jepsen, P.U., Cooke, D.G., Koch, M.: Terahertz spectroscopy and imaging – modern techniques and applications. *Laser & Photonics Reviews* **5**(1), 124–166 (2011). <https://doi.org/10.1002/lpor.201000011>
- [14] Xie, L., Yao, Y., Ying, Y.: The application of terahertz spectroscopy to protein detection: A review. *Applied Spectroscopy Reviews* **49**(6), 448–461 (2014). <https://doi.org/10.1080/05704928.2013.847845>
- [15] Neu, J., Schmuttenmaer, C.A.: Tutorial: An introduction to terahertz time domain spectroscopy (thz-tds). *Journal of Applied Physics* **124**(23), 231101 (2018). <https://doi.org/10.1063/1.5047659>
- [16] Hangyo, M., Tani, M., Nagashima, T.: Terahertz time-domain spectroscopy of solids: A review. *International Journal of Infrared and Millimeter Waves* **26**(12), 1661–1690 (2005). <https://doi.org/10.1007/s10762-005-0288-1>
- [17] Fischer, B., Hoffmann, M., Helm, H., Modjesch, G., Jepsen, P.U.: Chemical recognition in terahertz time-domain spectroscopy and imaging. *Semiconductor Science and Technology* **20**(7), 246–253 (2005). <https://doi.org/10.1088/0268-1242/20/7/015>
- [18] Bawuah, P., Zeitler, J.A.: Advances in terahertz time-domain spectroscopy of pharmaceutical solids: A review. *TrAC Trends in Analytical Chemistry*, 116272 (2021). <https://doi.org/10.1016/j.trac.2021.116272>
- [19] Hafez, H.A., Chai, X., Ibrahim, A., Mondal, S., Férachou, D., Ropagnol, X., Ozaki, T.: Intense terahertz radiation and their applications. *Journal of Optics* **18**(9), 093004 (2016). <https://doi.org/10.1088/2040-8978/18/9/093004>
- [20] Cook, D.J., Hochstrasser, R.M.: Intense terahertz pulses by four-wave rectification in air. *Opt. Lett.* **25**(16), 1210–1212 (2000). <https://doi.org/10.1364/OL.25.001210>
- [21] Kress, M., Löffler, T., Eden, S., Thomson, M., Roskos, H.G.: Terahertz-pulse generation by photoionization of air with laser pulses composed of both fundamental and second-harmonic waves. *Opt. Lett.* **29**(10), 1120–1122 (2004). <https://doi.org/10.1364/OL.29.001120>
- [22] Kim, K.Y., Glowina, J.H., Taylor, A.J., Rodriguez, G.: Terahertz emission from ultrafast ionizing air in symmetry-broken laser fields. *Opt. Express* **15**(8), 4577–4584 (2007). <https://doi.org/10.1364/OE.15.004577>
- [23] Kim, K.Y., Taylor, A.J., Glowina, J.H., Rodriguez, G.: Coherent control of terahertz supercontinuum generation in ultrafast laser-gas interactions. *Nature Photonics* **2**(10), 605–609 (2008). <https://doi.org/10.1038/nphoton.2008.153>

- [24] Matsubara, E., Nagai, M., Ashida, M.: Ultra-broadband coherent electric field from far infrared to 200 thz using air plasma induced by 10 fs pulses. *Applied Physics Letters* **101**(1), 011105 (2012). <https://doi.org/10.1063/1.4732524>
- [25] Karpowicz, N., Dai, J., Lu, X., Chen, Y., Yamaguchi, M., Zhao, H., Zhang, X.-C., Zhang, L., Zhang, C., Price-Gallagher, M., Fletcher, C., Mamer, O., Lesimple, A., Johnson, K.: Coherent heterodyne time-domain spectrometry covering the entire “terahertz gap”. *Appl. Phys. Lett.* **92**(1), 011131 (2008). <https://doi.org/10.1063/1.2828709>
- [26] Ho, I.-C., Guo, X., Zhang, X.-C.: Design and performance of reflective terahertz air-biased-coherent-detection for time-domain spectroscopy. *Opt. Express* **18**(3), 2872–2883 (2010). <https://doi.org/10.1364/OE.18.002872>
- [27] Prost, E., Loriot, V., Constant, E., Compagnon, I., Bergé, L., Lépine, F., Skupin, S.: Air-photonics terahertz platform with versatile micro-controller based interface and data acquisition. *Review of Scientific Instruments* **93**(3), 033004 (2022) <https://doi.org/10.1063/5.0082593>. <https://doi.org/10.1063/5.0082593>
- [28] Babushkin, I., Kuehn, W., Köhler, C., Skupin, S., Bergé, L., Reimann, K., Woerner, M., Herrmann, J., Elsaesser, T.: Ultra-fast spatiotemporal dynamics of terahertz generation by ionizing two-color femtosecond pulses in gases. *Phys. Rev. Lett.* **105**, 053903 (2010). <https://doi.org/10.1103/PhysRevLett.105.053903>
- [29] Dai, J., Xie, X., Zhang, X.-C.: Detection of broadband terahertz waves with a laser-induced plasma in gases. *Phys. Rev. Lett.* **97**, 103903 (2006). <https://doi.org/10.1103/PhysRevLett.97.103903>
- [30] Lu, X., Karpowicz, N., Zhang, X.-C.: Broadband terahertz detection with selected gases. In: *Advances in Optical Sciences Congress*, p. 4. Optica Publishing Group, ??? (2009). <https://doi.org/10.1364/NLO.2009.NWA4>
- <http://opg.optica.org/abstract.cfm?URI=NLO-2009-NWA4>
- [31] Kaltenecker, K.J., Kelleher, E.J.R., Zhou, B., Jepsen, P.U.: Attenuation of thz beams: A “how to” tutorial. *Journal of Infrared, Millimeter, and Terahertz Waves* **40**(8), 878–904 (2019). <https://doi.org/10.1007/s10762-019-00608-x>
- [32] Iwaszczuk, K., Andryieuski, A., Lavrinenko, A., Zhang, X.-C., Jepsen, P.U.: Terahertz field enhancement to the mv/cm regime in a tapered parallel plate waveguide. *Opt. Express* **20**(8), 8344–8355 (2012). <https://doi.org/10.1364/OE.20.008344>
- [33] Naftaly, M., Dudley, R.: Methodologies for determining the dynamic ranges and signal-to-noise ratios of terahertz time-domain spectrometers. *Opt. Lett.* **34**(8), 1213–1215 (2009). <https://doi.org/10.1364/OL.34.001213>
- [34] Kolesik, M., Moloney, J.V., Mlejnek, M.: Unidirectional optical pulse propagation equation. *Phys. Rev. Lett.* **89**, 283902 (2002)
- [35] Kolesik, M., Moloney, J.V.: Nonlinear optical pulse propagation simulation: From Maxwell’s to unidirectional equations. *Phys. Rev. E* **70**, 036604 (2004)
- [36] Bergé, L., Skupin, S., Nuter, R., Kasparian, J., Wolf, J.P.: Optical ultrashort filaments in weakly-ionized, optically-transparent media. *Rep. Prog. Phys.* **70**, 1633 (2007)
- [37] Bergé, L., Skupin, S.: Few-cycle light bullets created by femtosecond filaments. *Phys. Rev. Lett.* **100**, 113902 (2008)
- [38] Babushkin, I., Kuehn, W., Köhler, C., Skupin, S., Bergé, L., Reimann, K., Woerner, M., Herrmann, J., Elsaesser, T.: Ultra-fast spatiotemporal dynamics of terahertz generation by ionizing two-color femtosecond pulses in gases. *Phys. Rev. Lett.* **105**, 053903 (2010). <https://doi.org/10.1103/PhysRevLett.105.053903>
- [39] Tailliez, C., Stathopoulos, A., Skupin, S.,

- Buožiūsis, D., Babushkin, I., Vaičiūsis, V., Bergé, L.: Terahertz pulse generation by two-color laser fields with circular polarization. *New J. Phys.* **22**, 103038 (2020)
- [40] Nguyen, A., de Alaiza Martínez, P.G., Déchard, J., Thiele, I., Babushkin, I., Skupin, S., Bergé, L.: Spectral dynamics of thz pulses generated by two-color laser filaments in air: the role of kerr nonlinearities and pump wavelength. *Opt. Express* **25**, 4720 (2017)
- [41] Nguyen, A., Kaltenecker, K.J., Delagnes, J.-C., Zhou, B., Cormier, E., Fedorov, N., Bouillaud, R., Descamps, D., Thiele, I., Skupin, S., Jepsen, P.U., Bergé, L.: Wavelength scaling of terahertz pulse energies delivered by two-color air plasmas. *Opt. Lett.* **44**(6), 1488–1491 (2019). <https://doi.org/10.1364/OL.44.001488>
- [42] Tamošauskas, G., Beresnevičius, G., Gadonas, D., Dubietis, A.: Transmittance and phase matching of bbo crystal in the 3-5  $\mu\text{m}$  range and its application for the characterization of mid-infrared laser pulses. *Opt. Mater. Express* **8**(6), 1410–1418 (2018). <https://doi.org/10.1364/OME.8.001410>
- [43] Ghosh, G.: Dispersion-equation coefficients for the refractive index and birefringence of calcite and quartz crystals. *Optics Communications* **163**(1), 95–102 (1999). [https://doi.org/10.1016/S0030-4018\(99\)00091-7](https://doi.org/10.1016/S0030-4018(99)00091-7)
- [44] Zhang, Z., Panov, N., Andreeva, V., Zhang, Z., Slepko, A., Shipilo, D., Thomson, M.D., Wang, T.-J., Babushkin, I., Demircan, A., Morgner, U., Chen, Y., Kosareva, O., Savel'ev, A.: Optimum chirp for efficient terahertz generation from two-color femtosecond pulses in air. *Applied Physics Letters* **113**(24), 241103 (2018) <https://doi.org/10.1063/1.5053893>. <https://doi.org/10.1063/1.5053893>
- [45] Klarskov, P., Strikwerda, A.C., Iwaszczuk, K., Jepsen, P.U.: Experimental three-dimensional beam profiling and modeling of a terahertz beam generated from a two-color air plasma. *New Journal of Physics* **15**(7), 075012 (2013). <https://doi.org/10.1088/1367-2630/15/7/075012>
- [46] Oh, T.I., You, Y.S., Jhajj, N., Rosenthal, E.W., Milchberg, H.M., Kim, K.Y.: Intense terahertz generation in two-color laser filamentation: energy scaling with terawatt laser systems. *New Journal of Physics* **15**(7), 075002 (2013). <https://doi.org/10.1088/1367-2630/15/7/075002>
- [47] Andreeva, V.A., Kosareva, O.G., Panov, N.A., Shipilo, D.E., Solyankin, P.M., Esaulkov, M.N., González de Alaiza Martínez, P., Shkurinov, A.P., Makarov, V.A., Bergé, L., Chin, S.L.: Ultrabroad terahertz spectrum generation from an air-based filament plasma. *Phys. Rev. Lett.* **116**, 063902 (2016). <https://doi.org/10.1103/PhysRevLett.116.063902>
- [48] Shipilo, D.E., Panov, N.A., Nikolaeva, I.A., Ushakov, A.A., Chizhov, P.A., Mamaeva, K.A., Bukin, V.V., Garnov, S.V., Kosareva, O.G.: Low-frequency content of thz emission from two-color femtosecond filament. *Photonics* **9**(1) (2022). <https://doi.org/10.3390/photonics9010017>
- [49] Gordon, I.E., Rothman, L.S., Hargreaves, R.J., Hashemi, R., Karlovets, E.V., Skinner, F.M., Conway, E.K., Hill, C., Kochanov, R.V., Tan, Y., Wcisło, P., Finenko, A.A., Nelson, K., Bernath, P.F., Birk, M., Boudon, V., Campargue, A., Chance, K.V., Coustenis, A., Drouin, B.J., Flaud, J.-M., Gamache, R.R., Hodges, J.T., Jacquemart, D., Mlawer, E.J., Nikitin, A.V., Perevalov, V.I., Rotger, M., Tennyson, J., Toon, G.C., Tran, H., Tyuterev, V.G., Adkins, E.M., Baker, A., Barbe, A., Canè, E., Császár, A.G., Dudaryonok, A., Egorov, O., Fleisher, A.J., Fleurbaey, H., Foltynowicz, A., Furtenbacher, T., Harrison, J.J., Hartmann, J.-M., Horneman, V.-M., Huang, X., Karman, T., Karns, J., Kass, S., Kleiner, I., Kofman, V., Kwabia-Tchana, F., Lavrentieva, N.N., Lee, T.J., Long, D.A., Lukashchuk, A.A., Lyulin, O.M., Makhnev, V.Y., Matt, W., Massie, S.T., Melosso, M., Mikhailenko, S.N., Mondelain, D., Müller, H.S.P., Naumenko, O.V., Perrin, A., Polyansky, O.L.,

- Raddaoui, E., Raston, P.L., Reed, Z.D., Rey, M., Richard, C., Tóbiás, R., Sadiék, I., Schwenke, D.W., Starikova, E., Sung, K., Tamassia, F., Tashkun, S.A., Auwera, J.V., Vasilenko, I.A., Vigasin, A.A., Villanueva, G.L., Vispoel, B., Wagner, G., Yachmenev, A., Yurchenko, S.N.: The hitran2020 molecular spectroscopic database. *Journal of Quantitative Spectroscopy and Radiative Transfer*, 107949 (2021). <https://doi.org/10.1016/j.jqsrt.2021.107949>
- [50] Ardana-Lamas, F., Erny, C., Stepanov, A.G., Gorgisyan, I., Juranić, P., Abela, R., Hauri, C.P.: Temporal characterization of individual harmonics of an attosecond pulse train by thz streaking. *Phys. Rev. A* **93**, 043838 (2016). <https://doi.org/10.1103/PhysRevA.93.043838>
- [51] Xu, L., Tutunnikov, I., Gershnel, E., Prior, Y., Averbukh, I.S.: Long-lasting molecular orientation induced by a single terahertz pulse. *Phys. Rev. Lett.* **125**, 013201 (2020). <https://doi.org/10.1103/PhysRevLett.125.013201>
- [52] Tcypkin, A., Zhukova, M., Melnik, M., Vorontsova, I., Kulya, M., Putilin, S., Kozlov, S., Choudhary, S., Boyd, R.W.: Giant third-order nonlinear response of liquids at terahertz frequencies. *Phys. Rev. Applied* **15**, 054009 (2021). <https://doi.org/10.1103/PhysRevApplied.15.054009>